Upcycling end-of-life bricks in high-performance one-part alkali-activated materials

Yazeed A. Al-Noaimat [a], Mehdi Chougan [a], Mazen J. Al-kheetan [b], Marcus H.N. Yio [c], Hong S. Wong [c], Seyed Hamidreza Ghaffar [a,d,*]

[a] *Department of Civil and Environmental Engineering, Brunel University, London, Uxbridge, Middlesex, UB8 3PH, United Kingdom*
[b] *Department of Civil and Environmental Engineering, College of Engineering, Mutah University Mutah, Karak, 61710, P.O. BOX 7, Jordan*
[c] *Centre for Infrastructure Materials, Department of Civil and Environmental Engineering, Imperial College London, London, SW7 2AZ, United Kingdom*
[d] *Applied Science Research Center, Applied Science Private University, Jordan*

ARTICLE INFO

ABSTRACT

One-part alkali-activated materials (AAMs) can preserve natural resources and lower embodied carbon of the built environment by accommodating various wastes, industrial by-products, and end-of-life materials in their composition. This study investigates the feasibility of using end-of-life bricks in two physical states, powder and aggregate, to partially replace fly ash precursor and natural aggregate in AAMs, respectively. The mechanical characteristics, microstructure, water absorption, freeze-thaw and fire resistance of the modified AAMs were evaluated. The effect of adding different ratios of nano graphite platelets was also investigated. Results showed that brick-based one-part AAMs can achieve mechanical properties, pore structure, water absorption and freeze-thaw resistance comparable to fly ash-based AAM while having 65% better fire resistivity. Incorporating bricks as aggregate resulted in a maximum improvement of 17% and 27% in the AAMs' compressive and flexural strength levels, respectively, and a general enhancement in the freeze-thaw resistance with showing no reduction in compressive strength after exposure to elevated temperature. Incorporating 0.1 wt% nano-graphite further enhanced flexural strength by 30%, decreased water absorption by 18% and improved freeze-thaw resistance compared to the mix without nano-graphite. Moreover, adding up to 0.5% nano-graphite enhanced the fire resistivity of the composite, allowing it to exhibit 19% better strength performance than before exposure.

1. Introduction

The overutilisation of natural resources and massive greenhouse gas emissions associated with construction activities are major issues that need to be tackled urgently in our drive to achieve sustainable development. In this regard, addressing the ever-increasing demand for Portland cement and natural aggregates for concrete is critical. Portland cement production is a high-energy process that involves heating raw natural resources at approximately 1450 °C and this releases CO_2 that contributes to approximately 8% of global anthropogenic emissions (Juenger et al., 2011; Al-noaimat et al., 2023a; Akis, 2023). A potentially sustainable alternative to Portland cement is alkali-activated materials (AAMs). These are produced by combining aluminosilicate-rich precursor materials with an alkaline activator (in liquid or solid form) to induce geopolymerisation, forming a solid binder. The various properties of two-part AAMs, including their fresh, hardened, printing

properties and durability have been comprehensively investigated and found to have superior mechanical performance to that of OPC-based concrete (El-seidy et al., 2023; El-seidy et al., 2022; Chindaprasirt et al., 2011). However, some limitations were also found for its application for large-scale, including shrinkage (Zhang et al., 2022). In the last decade, one-part "just add water" AAMs composed of solid powder alkaline activators have been developed to mitigate health and safety risks associated with the use of alkaline solutions on-site (Duxson et al., 2007; Erfanimanesh and Sharbatdar, 2020; Al-noaimat et al., 2023b).

Meanwhile, increasing developmental construction activities have generated massive volumes of construction and demolition waste (CDW) globally. In 2018 alone, China, the United States and India generated approximately 2.36 billion, 600 million, and 530 million tonnes of CDW, respectively (Wang et al., 2021). CDWs are responsible for almost 30% of worldwide solid waste, the vast majority of which is landfilled, causing substantial negative environmental impacts (El-seidy et al.,

2022; Dadsetan et al., 2019; Lu, 2019; Robayo et al., 2016). Depending on the type of demolished structure, CDWs contain mainly concrete, steel and bricks. These can be reclaimed and recycled to be used in new construction, thereby reducing the problems associated with waste treatment and disposal and the construction industry's over-dependence on natural raw materials. Incorporating recycled concrete as aggregate in new concrete has been studied extensively (Liu et al., 2019). However, the incorporation of recycled bricks aggregates (BA) is limited due to their higher porosity compared to concrete aggregates (Paul et al., 2018). On the one hand, some studies have reported negative effects of BA, such as increasing water absorption and chloride ion diffusion (Dang et al., 2018). On the other hand, studies have also reported positive effects such as improved acoustic and thermal insulation (Dang et al., 2018) and lower drying shrinkage due to moisture held in the pore structure of the brick (Zhang et al., 2018; Wong et al., 2018). The main environmental benefit of replacing natural aggregate with BA is to limit the depletion of natural resources (Robert, 2020), but many outstanding questions regarding the performance of concrete containing recycled brick aggregates remain.

The valorisation of waste materials rich in silica and alumina, such as brick, as precursors in AAMs has been gaining interest in recent years. Bricks contain high Al_2O_3 and SiO_2, similar in composition to supplementary cementitious materials (SCMs) such as fly ash. Therefore, some studies have investigated the feasibility of using end-of-life bricks as a binder replacement in concrete and alkali-activated materials (Arif et al., 2021; Rovnaník et al., 2018; Bayraktar et al., 2019a, 2019b). Ma et al. (2020) reported that replacing up to 30% Portland cement with brick powder (BP) resulted in comparable mechanical performance to a standard mortar. Increasing the BP fineness also decreased the mortars' water absorption and enhanced its compressive strength due to the more significant filler effect and pozzolanic reactivity of BP. Similarly, Wong et al. (2020a) found that a fly ash-based two-part AAM prepared with 10% BP had around 20% higher compressive strength than the control AAM. The incorporation of up to 20% BP decreased the porosity and water absorption of the AAM due to the filler effect.

Improving the performance of cementitious materials with carbon-based nanoparticles (such as graphene nanoplatelets, nano graphite platelets, graphene oxide, reduced graphene oxide, and carbon nanotube) has drawn much attention due to their superior Young's modulus and tensile strength (Zheng et al., 2017; Mackenzie and Bolton, 2009). Chougan et al. (2020a) studied the effect of incorporating different dosages of nano graphite platelets (i.e., 0.1, 0.3, 0.5, 1% by binder) on the properties of 3D printed AAM and reported up to 89% and 28% enhancement in flexural and compressive strength, respectively. Several applications for cementitious composites containing nano graphite particles have been suggested, including increased thermal conductivity for de-icing roads, high-voltage transmission pipelines, and under-floor heating (Liu et al., 2016; Dimov et al., 2018), and increased electrical conductivity to induce self-sensing properties for structural health monitoring (Papanikolaou et al., 2021). Considering the mass production of graphene-based materials (GBM), the price of these products significantly dropped over the past few years (Chougan et al., 2019). It should be noted that these materials are proven to be safe for both human health and the environment (Fadeel et al., 2018). It is worth noting that safety measures should be taken when working with nanomaterials and powder activators (i.e., special face mask and gloves). For instance, Papanikolaou et al. (2021) evaluated the environmental impact of concrete reinforced with graphene nanoplatelets, focusing on the "cradle-to-gate" of GBM production and their incorporation in cementitious composites. According to their study, producing 1 kg of graphene nanoplatelets (GNPs) from the same supplier used in this research results in much lower carbon dioxide emissions (0.17 $kgCO_2$ equivalent) compared to producing the same amount of Portland cement (0.86 $kgCO_2$ equivalent). This suggests that GBMs could be a more environmentally friendly option if used as an additive. Their results also indicated that incorporating GBMs is a crucial step towards reducing the

binder content required for concrete while maintaining/enhancing its performance, as the sensitivity analysis revealed that adding 2 wt% GNPs led to a 5% reduction in Portland cement usage, ultimately resulting in a remarkable 21% decrease in the concrete mix's impact on global warming.

This study investigates the potential of upcycling end-of-life bricks in powder form as a replacement to fly ash precursor and in aggregate form as an alternative to natural aggregate in one-part "just-add-water" alkali-activated materials. This study contributes to the state-of-the-art by investigating the feasibility of combining brick as a binder and aggregate in the same mixture to decrease the high amount of yearly disposed end-of-life materials, and limit the over dependency on the limited sources, such as natural aggregate and industrial by-products (i.e., fly ash). There are three phases in this work. The first phase examines the effect of replacing fly ash (FA) with brick powder (BP) on reaction kinetics, microstructure and strength performance. The second phase examines the effect of replacing natural aggregate with brick aggregate (BA), and finally, the best-performing mixture is taken forward to study the potential of incorporating nano-graphite (nG) as a means to enhance the properties of waste brick-based AAMs. The durability of selected mixes is assessed by conducting water absorption and freeze-thaw tests. It is important to mention that the utilisation of nanographite platelets was just one aspect of the study aimed at exploring the capabilities of carbon-based materials in developing high-performance alkali-activated materials. To the best of the authors' knowledge, the combined effects of replacing FA precursor and natural aggregate with waste brick, and the addition of nano graphite platelets in one-part AAM have not been reported before. Thus, this study represents a unique contribution to the current state-of-the-art.

2. Materials and methods

A schematic overview of the experimental programme is presented in Fig. 1.

2.1. Materials

Class F fly ash (FA) conforming to BS EN 450–1:2012 (BS EN 450-1, 2012) (Cemex, UK), ground-granulated blast furnace slag (GGBS) (Hanson, UK) and brick powder processed from end-of-life bricks collected from a demolition site near Brunel University London were used as precursors. Sodium metasilicate (SS) powder (Na_2SiO_3) with a SiO_2/Na_2O alkali modulus of 1.6 and purity of 99% (Fisher Scientific, UK) was used as the alkali activator. Nano-graphite platelets (nG) Grade K6Nan with a purity of 97.5% and 6–7 nm lamella thickness index were obtained from Nanesa srl., Italy. A detailed characterisation of the nano-graphite material has been reported in the authors' previous studies (Chougan et al., 2020a, 2020b). The collected bricks were crushed manually using a hammer, followed by automatic crushing using a 100 grinder machine (Retsch, Germany) equipped with a 2 mm mesh. Particles between 1 and 2 mm were sieved to obtain brick aggregate (BA). The residue material was further crushed and ground using a ball mill (Retsch, Germany) containing 8 ball for 5 min with a speed of 500 rpm, followed by sieving through a 125 μm mesh to obtain brick powder (BP). Fig. 2 presents the preparation process for BA and BP.

The XRF oxide composition and XRD patterns of FA, GGBS, and BP are given in Table 1 and Fig. 3a, respectively. The chemical compositions of BP and FA are comparable for most oxides. The results show that GGBS and FA are highly amorphous, with the latter containing traces of quartz and mullite. The predominant phase in BP was quartz due to the presence of SiO_2 in clay minerals and the incorporation of sand in brick manufacturing (Zawrah et al., 2016). The crystallinity index (CI) of FA and BP was determined using Rietveld method and was found to be 50% for FA and 70% for BP. Micrographs from scanning electron microscopy (SEM) in Fig. 4 show that the brick powder and brick aggregate are irregularly shaped with rough surface texture due to crushing. The
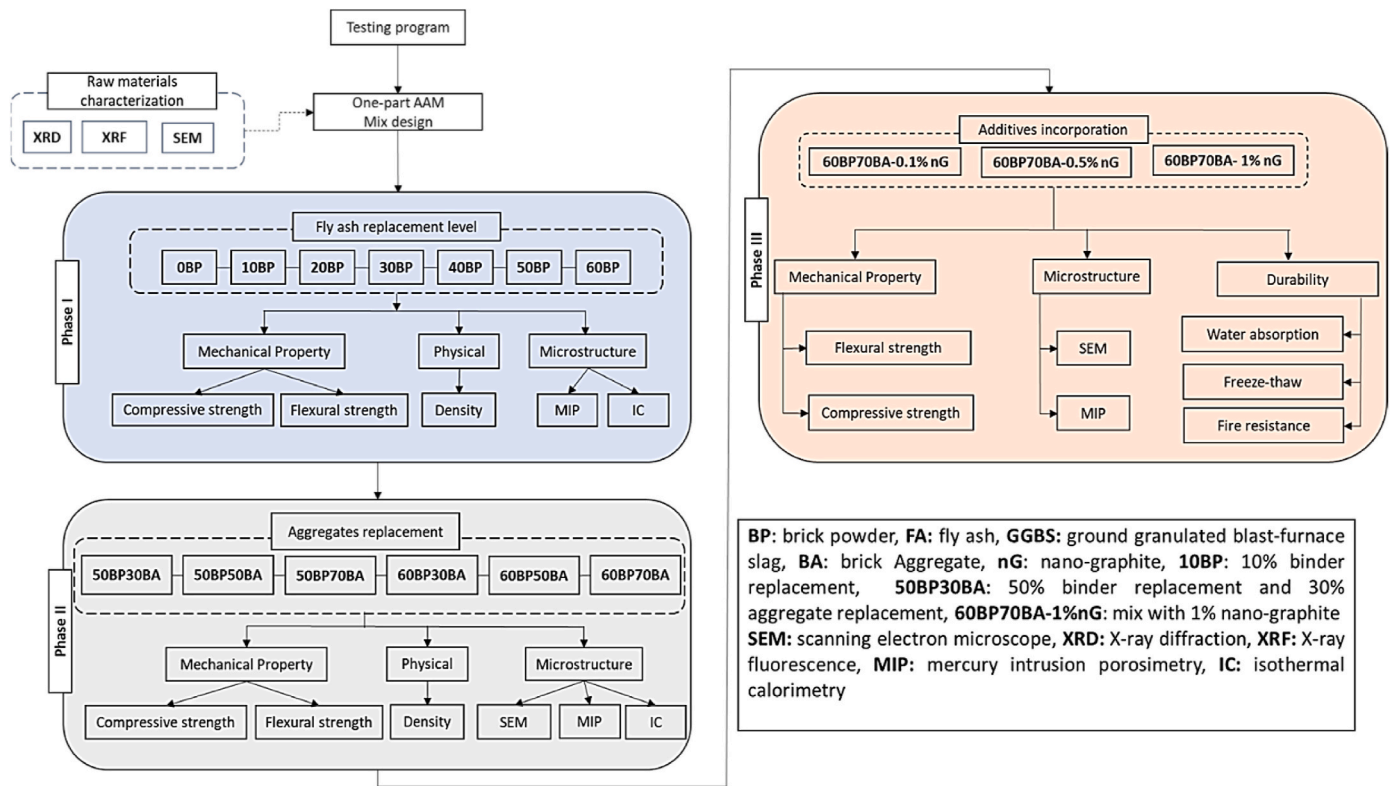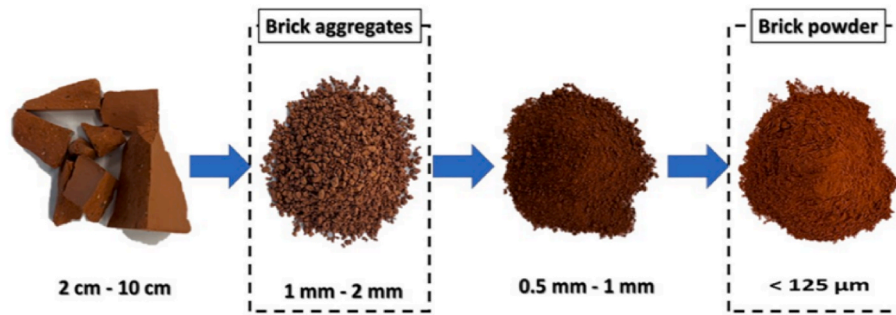
Fig. 1. Experimental test program.

Fig. 2. Brick powder and brick aggregate preparation process.

Table 1
Oxide compositions (wt. %) of FA, BP and GGBS obtained from XRF.

Material	SiO$_2$	Al$_2$O$_3$	CaO	Fe$_2$O$_3$	MgO	K$_2$O	SO$_3$	TiO$_2$	Na$_2$O LOI
FA	53.12	23.83	3.82	8.36	1.50	2.51	1.16	0.81	1.10 1.9
GGBS	26.75	9.31	49.05	0.73	7.42	0.40	2.65	0.61	0.30 1.2
BP	64.6	13.1	0.44	7.04	–	2.16	0.62	1.31	- 2.9

particle size distribution of the raw materials determined using laser granulometry is presented in Fig. 3b. The true particle densities of FA, BP, BA and natural aggregate were 1.99, and 2.44 g/cm^3, respectively. The density of GGBS complied with EN15167-1 (BS EN 15167-1, 2006) of approximately 2.4–3 g/cm^3. The densities of natural aggregate and BA were comparable, i.e., 1.98 and 1.82 g/cm^3, respectively. River sand (<2 mm) was combined with quartz sand (0.06–0.3 mm) (proportion of river sand and quartz sand detailed in Table 2) for use as natural aggregates. The aggregate size distribution of natural aggregates and BA determined using sieve analysis are illustrated in Fig. 3c.

2.2. Mix formulations and sample preparation

A total of 16 different one-part AAM formulations were prepared and investigated in three phases, as shown in Table 2. Preliminary investigations consisting of flexural strength, compressive strength, and setting time were conducted to optimise base mixture precursor. The results showed that although increasing GGBS content enhanced the mechanical performance of the mixture, setting time decreased. Accordingly, 60% FA and 40% GGBS was selected as the base mixture formulation because of the high mechanical performance and acceptable setting time. The binder in all mixes had a constant 40% GGBS, with
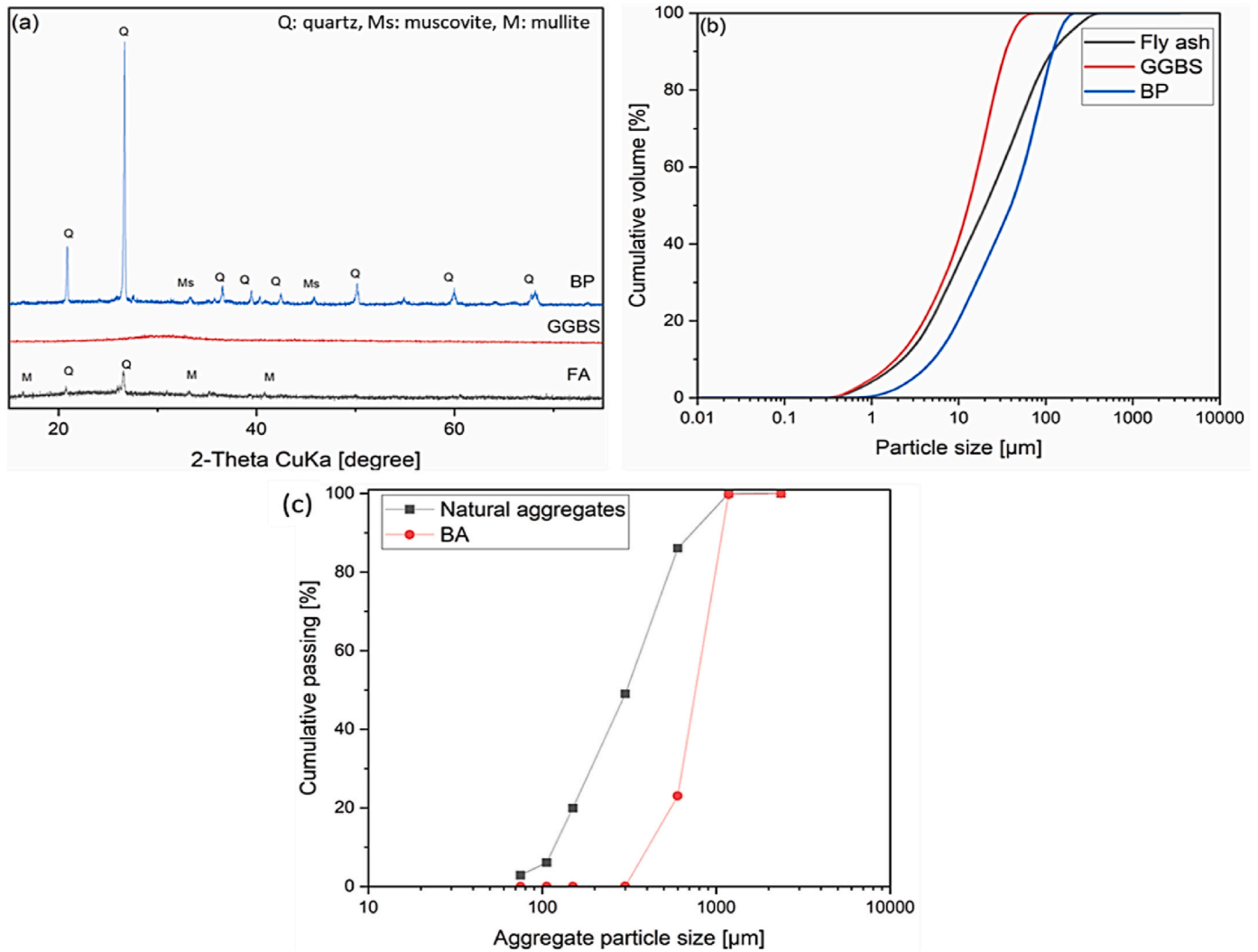
Fig. 3. (a) XRD pattern, (b) particle size distribution of FA, GGBS and BP and (c) particle size distribution of BA and natural aggregates.
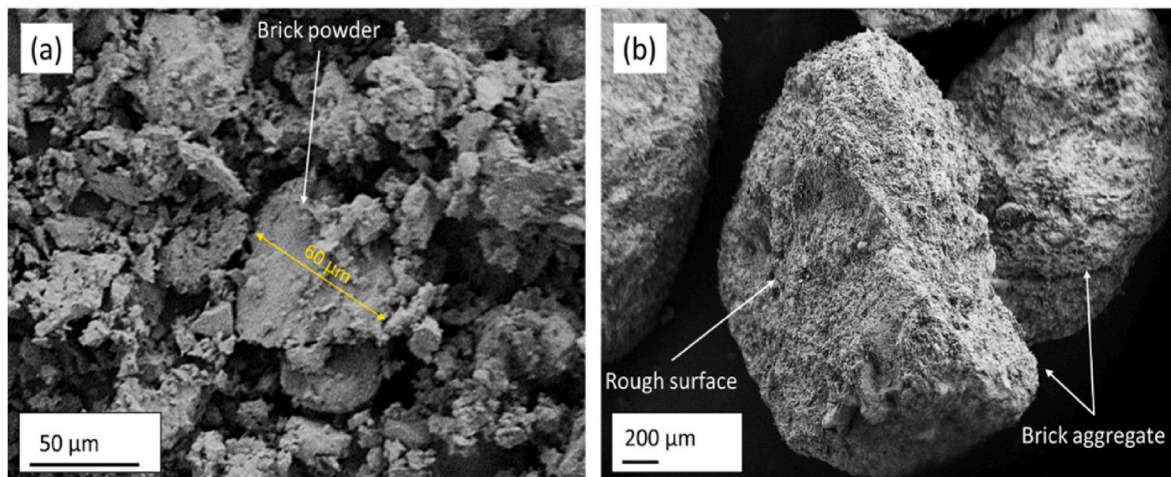

Fig. 4. SEM images of (a) BP and (b) BA.

the remaining 60% being a combination of FA and BP at 10% increment. Sodium silicate (SS) was used as the activator at 12% weight of the binder. Water-to-binder mass ratio of 0.4 was used for all mixtures. The water absorption of the aggregates was 9.8% and 0.8% for BA and sand,

respectively, determined according to ASTM C-128 (Statements and Size, 2003). The aggregate-to-binder ratio was set to 1.2. In phase II, the natural aggregates were replaced with 30%, 50%, and 70% BA. In phase III, nano-functionalised graphite platelets (nG) were added at 0.1%,

Table 2
Mix formulations for the three phases of material investigations.

	Mixture ID	Binder (wt.%)			Aggregates (wt.%)			SS (wt.%)	nG (wt.%)
		FA	GGBS	BP	River sand	Quartz sand	BA		
Phase I	0BP	60	40	–	85.3	14.7	–	12	–
	10BP	50	40	10	85.3	14.7	–	12	–
	20BP	40	40	20	85.3	14.7	–	12	–
	30BP	30	40	30	85.3	14.7	–	12	–
	40BP	20	40	40	85.3	14.7	–	12	–
	50BP	10	40	50	85.3	14.7	–	12	–
	60BP	–	40	60	85.3	14.7	–	12	–
Phase II	50BP30BA	10	40	50	59.7	10.3	30	12	–
	50BP50BA	10	40	50	42.65	7.35	50	12	–
	50BP70BA	10	40	50	25.59	4.41	70	12	–
	60BP30BA	–	40	60	59.7	10.29	30	12	–
	60BP50BA	–	40	60	42.65	7.35	50	12	–
	60BP70BA	–	40	60	25.59	4.41	70	12	–
Phase III	60BP70BA-0.1 nG	–	40	60	25.59	4.41	70	12	0.1
	60BP70BA-0.5 nG	–	40	60	25.59	4.41	70	12	0.5
	60BP70BA-1 nG	–	40	60	25.59	4.41	70	12	1

0.5%, and 1% weight of the binder. The mixtures were prepared in two stages. First, the solid ingredients (GGBS, FA, BP, SS, sand, BA, and nG) were dry-mixed for 3 min. After dry-mixing, tap water was gradually added for a duration of 2 min and mixed for an additional 8 min. For AAMs reinforced with nano-graphite platelets, nG was dispersed in water for 30 min using an ultrasonic homogeniser (U.S. solid, United States). At the end of the mixing process, specimens were cast in prismatic polystyrene moulds (40 x 40 x 160 m³), heat cured at 60 ℃ for 24 h, then de-moulded and kept in a room environment (20 ± 3 ℃ and 50% RH) until testing.

2.3. Experimental tests

2.3.1. Mechanical properties

Flexural strength (3-point bending) and compressive strength were measured after 3-days of curing following BS EN 196–1 (BS EN 196-1, 2016). The tests were performed using a Universal Testing System (Instron 5960) at a loading rate of one mm/min on prismatic samples of 160 x 40 × 40 mm. The flexural and compressive strength results were reported as the average of three and six replicates per mixture, respectively, and the standard deviations were calculated and presented as error bars. The coefficient of varience (CoV) was calculated for the obtained results.

2.3.2. Flowability

The workability differences between FA and the mixtures containing different ratios of BP were investigated by conducting the flow table test following BS EN 1015:3–1999 (BS EN 1015-3, 1999). The flowability of the mixtures was determined immediately at the end of the mixing process. The flow diameter readings were taken at 0, 5, 10, and 15 min.

2.3.3. Mercury intrusion porosimetry

Pore structure was characterised via mercury intrusion porosimetry using a Quantachrome Poremaster 60. Samples of approximately one cm³ were placed into the penetrometer assembly, de-aired and filled with mercury up to a pressure of 0.34 MPa in the low-pressure station. The assembly was then transferred to the high-pressure station where pressure was increased to 414 MPa, allowing the detection of pore sizes of down to 3.6 nm, assuming a mercury contact angle of 140°.

2.3.4. Isothermal calorimetry

The reaction kinetics was followed via isothermal calorimetry using a TA Instruments TAM Air calorimeter at 25 °C for 72 h. Five g sample was mixed externally for 10 min, then transferred to a 20 ml glass ampoule and loaded into the calorimeter. The measured heat flow data were normalised to the total mass of the binder. Data from the first 45

min were discarded due to disturbance caused by external mixing.

2.3.5. Microstructure analysis

The microstructure of one-part AAMs was studied using scanning electron microscopy (SEM) (Supra 35VP, Carl Zeiss, Germany) equipped with energy-dispersive X-ray spectroscopy (EDS) (EDAX, USA). The analysis was conducted on small fractured pieces collected from mortar prisms after flexural testing with approximate dimensions of 6 x 6 × 6 mm. Prior to SEM analysis, the samples were gold coated using an Edwards S150B sputter coater to prevent surface charging effects. Around 15 secondary electron images were taken from each sample at a varying accelerating voltage of five to seven kV to ensure meaningful observations. EDS spot analysis was performed on seven randomly selected regions on a polished paste piece to calculate the Si/Al ratios. The results were averaged, and standard deviation calculated.

2.3.6. X-ray diffraction

0BP and 60BP pastes were prepared for investigation by dry mixing the binder and activator for 3 min, followed by adding water and wet mixing for 10 min. The samples were cured in the same manner as the mortar samples and then ground into fine powder for analysis. XRD measurements were conducted using a Malvern Panalytical Empyrean XRD in the Bragg-Brentano geometry with CuKα radiation (λ = 1.540596 Å). The incoming beam path had a programmable divergence slit, while the diffracted beam path had a programmable anti-scatter slit. Each scan was conducted in the 2θ range of 10°–75° within a measurement period of 1 h.

2.3.7. Water absorption

Water absorption was carried out according to BS 1881–122:2011 (BS 1881-122, 2011) as a performance indicator for durability (Wang et al., 2019; Li et al., 2020; Pandey and Kumar, 2019). The test was conducted on 3-day cured prismatic samples (40 x 40 × 160 mm). Samples were oven-dried at 105 °C for 48 h, weighed, and then submerged in water, and their mass was measured periodically until saturation. The water absorption (%) was calculated as follows:

$$Water\ absorption\ (\%) = \frac{M_t - M_0}{M_0} \times 100 \tag{1}$$

Where M_t (g) represents the sample mass at time t after exposure to water, and M_0 (g) represents the oven-dried mass.

2.3.8. Freeze-thaw resistance

Freeze-thaw (FT) resistance was determined on 3-day cured prismatic specimens (40 x 40 × 160 mm) following the Polish standard PN-85-B-04500 (PN-85/B-04500, 1985). The specimens were submerged in

water for 24 h and then placed in the FT chamber for 25 FT cycles at 98 %RH. Each cycle involved 4 h of freezing at −20 ˚C, followed by 4 h of thawing at 20 ˚C. Compressive strength test was performed on the samples at the end of 25 FT cycles to determine the strength loss calculated as:

$$Strength\ reduction\ (\%) = \frac{C_1}{C_0} \times 100 - 100 \qquad (2)$$

Where C_0 is the compressive strength of the normal cured mixture and C_1 is the compressive strength of the mixture after exposure to the FT cycles.

2.3.9. Fire resistance

Fire resistivity was investigated on the control sample as well as the mixtures selected as the best-performing mix from each phase by exposing the specimens at the age of 3 days to a temperature of 800 °C for 1 h using a CARBOLITE CWF 1100 furnace with a gradual temperature increment of 10 °C/min from the ambient temperature to the target temperature. At the end of the exposure time, the furnace was turned off, and the samples were left to cool down in the furnace to room temperature under open-air conditions. Then, their mechanical performance was investigated.

3. Results and discussions

3.1. Effect of replacing fly ash with brick powder

Fig. 5 presents the mechanical properties of the mixtures as a function of increasing replacement levels of brick powder (BP). Fig. 5a shows that all mixtures containing BP exhibited 6–15% lower flexural strength than the control sample (7.5 MPa), where 20BP had the lowest flexural strength of 6.4 MPa. However, it is worth noting that the amount of reduction in flexural strength did not correlate to the replacement level. All the mixtures have CoV less than 6%. Similarly, substituting FA with BP reduced the compressive strength relative to the control (0BP). 10BP showed the lowest compressive strength of 33 MPa, which was 20% lower than the control. The lower compressive strength of 10BP could be associated with the high flowability of the mix, as shown in Fig. 5b, which indicates the presence of higher amount of free water in the materials, resulting in an increase in pore size and volume. This observation is also confirmed by MIP, as shown in Fig. 6 that presents the cumulative and first derivative curves from MIP. Fig. 6a shows that 10BP had a higher pore volume than 0BP and 60BP. In addition, the critical pore diameter was slightly larger than those of 0BP and 60BP (Fig. 6b). These results correlate with the compressive strength results.

Interestingly, increasing the replacement level of fly ash beyond 10% with BP led to gradual increase in the compressive strength of AAM. For example, 60BP had a compressive strength of 38 MPa, which is around 16% higher than the 10BP (33 MPa). The results of the different samples had a CoV less than 4%. The increase in compressive strength with increasing BP content could be attributed to the decline in flowability (see Fig. 5b), indicating the better compaction of the mixtures and lower porosity. The flowability of the mixture is mainly governed by two factors, which are the shape and fineness of the particles. The highly irregular shape and rough surface of BP particles contribute to the decrease in the flowability of the mixture, in contrast to those of the spherical FA particles (Chindaprasirt et al., 2011; Wong et al., 2020b). However, the results of the current study suggest that, up to a certain replacement level (i.e., 30%), the fineness effect of binder materials is dominant over the shape effect on the flowability of the mixtures. Mixtures prepared with more than 30% of BP had slightly lower flowability than the control mixture (0BP), indicating that BP's shape and porous nature became dominant over the fineness of FA, as shown in Fig. 5b. This observation is in good agreement with MIP test results, which showed that 60BP has lower porosity and smaller critical pore diameter than 10BP (see Fig. 6).

The density of mixtures slightly increased with increasing BP content. The compressive strength of a mixture generally improves when its density increase since the higher density denotes lower voids content. However, the density difference between the mixes before and after BP substitution is negligible (1.9 g cm^{-3} for 0BP and 2.04 g cm^{-3} for 60BP) and can be attributed to the higher density of BP (i.e., 2.445 g cm^{-3}) compared to FA (i.e., 1.995 g cm^{-3}).

Fig. 7 shows the XRD patterns of 0BP and 60BP pastes cured for 3-days. As expected, the main crystalline phase was quartz (Q), derived from raw brick powder (Fig. 3a). 60BP showed a high peak intensity at 26.6˚ due to the high amount of quartz presented in BP, which notably decreases the reactivity of the fraction-bearing Al–Si (Álvarez-Ayuso et al., 2008). This high crystallinity nature of BP (i.e., 70%, see Section 2.1) prevents the particles' complete dissolution and participation in the alkali reaction, lowering the amount of hydration product formed. That could explain the slight reduction in the mechanical strength values of the 60BP mix compared to that of the control sample (0BP). To better understand the effect of crystalline phases on the mechanical property of the mixture, the Si/Al ratio of 0BP and 60BP pastes were determined using EDS on polished paste pieces. Results showed that the Si/Al ratio of 60BP (i.e. 4.1 ± 0.1) was significantly higher than that of 0BP (i.e., 2.8 ± 0.04) due to the presence of more quartz in the mixture. According to Yusuf et al. (2014), excessively high Si/Al ratios (i.e., higher than 3.8) can impair the mechanical performance of the resulting mixture due to excessive production of aluminosilicate gel in the very early stages of the
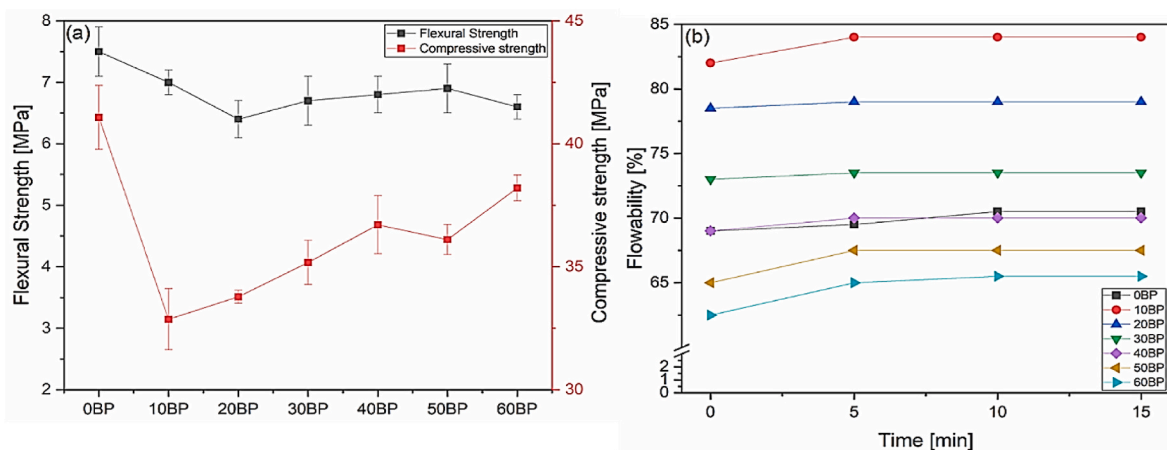

Fig. 5. Effect of replacing different percentages of FA with BP on (a) flexural strength and compressive strength and (b) flowability of one-part AAM mixes. Error bars represent the standard deviation.
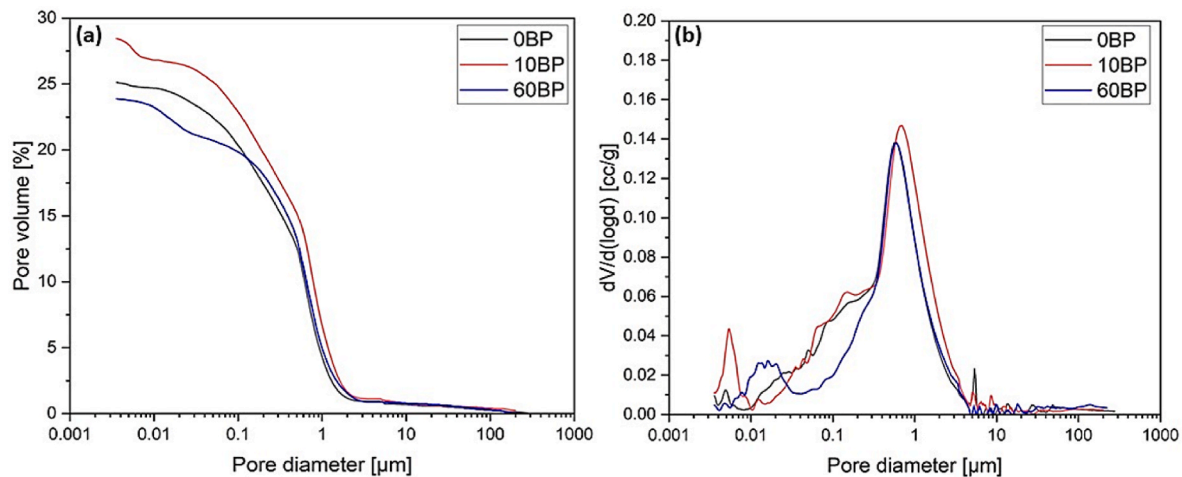
Fig. 6. (a) Cumulative intrusion and (b) pore size distribution from MIP.
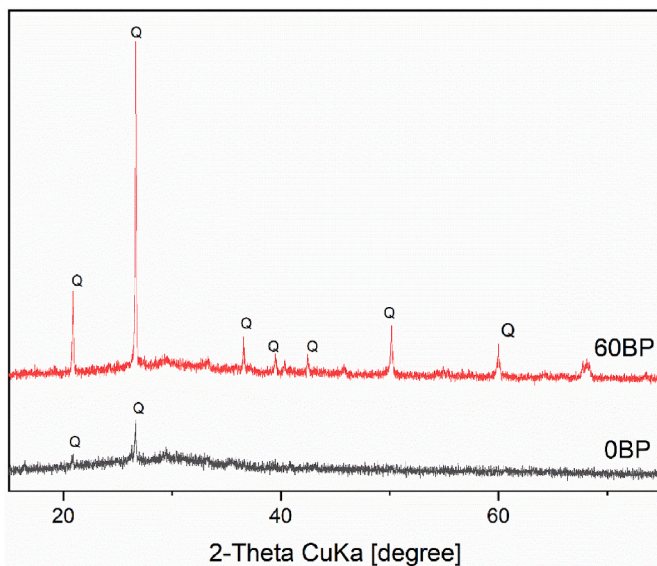

Fig. 7. XRD patterns of 0BP and 60BP mixes (Q: quartz).

reaction, which prevents proper subsequent development of micro-structure (Criado et al., 2007). The strength reduction between 0BP and 60BP can therefore be associated with the higher crystalline content and the significant increase in the Si/Al ratio.

The differences in reaction kinetics between 0BP and 60BP in the first 72 h were studied using isothermal calorimetry. Fig. 8 shows that the heat flow curves are composed of five stages: (1) dissolution (Peak I), (2) dormant (i.e., the period between the deceleration of the first exothermic peak and the beginning of the second exothermic peak), (3) acceleration (Peak II), (4) deceleration, and (5) steady state (Ma et al., 2022). The dissolution peak (I) for 60BP was higher and occurred earlier (Fig. 8 a(i)) compared to the control. This could be due to the higher silicate content in BP compared to FA (Table 1). Moreover, the acceleration peak (II) of 60BP was also seen to occur earlier and at a slightly higher intensity than 0BP (Fig. 8 aii). These results indicated faster dissolution and the earlier reaction of the dissolved ions in the geo-polymerisation process of 60BP. The results are in good agreement with those of EDS, which proves the promotion of gel formation (i.e., acceleration in peak II) in the presence of an excessive Si/Al ratio, as discussed before. Following the deceleration of peak II, the mixtures presented similar heat release behaviour. The reaction kinetics of AAM binders can be reflected through the total heat release during the first 72 h reaction. The results demonstrated the comparable reactivity of BP to that of FA, where both mixtures exhibited similar behaviour. However, 60BP had considerably higher total heat released after 72 h than 0BP, as
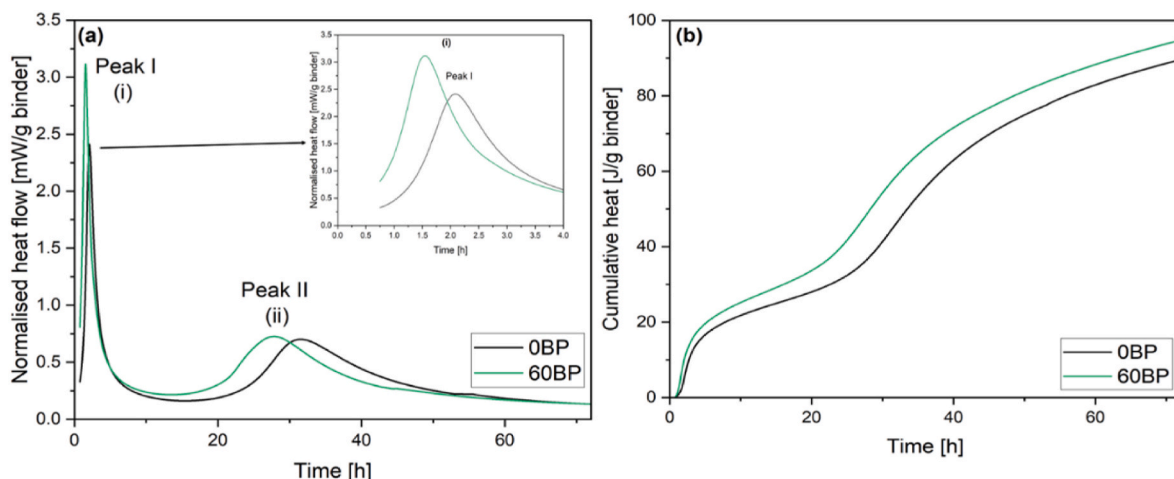

Fig. 8. Isothermal calorimetry curves of one-part AAMs: (a) normalised heat flow and (b) cumulative heat release.

shown in Fig. 8b.

Other researchers have studied the effect of incorporating brick powder to replace part of the precursor. These studies have shown similar or better mechanical performance than the control mixes (Migunthanna et al., 2021; Hwang et al., 2019). Nevertheless, due to differences in the bricks and mix formulations, a limited comparison can be made between this study and the results obtained in other studies. For example, Migunthanna et al. (2021) achieved a slightly higher compressive strength than the results presented here after three days, reaching around 43 MPa when using the same precursor formulation (i. e., 60% BP, 40% GGBS) but with a 10% liquid activator in a two-part AAM. Hwang et al. (2019) attained compressive strength up to 50 MPa after three days for mortar containing 60% BP and 40% GGBS in a two-part AAM. Collectively, these studies and the present work show that incorporating BP in AAM is a promising approach, and the mechanical properties indicate that the reactivity of BP is comparable to FA. The mechanical results show that a further increase in BP content in the mixture is possible. However, it was limited to replacing FA in the presented study to maintain high strength performance. As a cementitious material, BP presents a suitable alternative to FA, exhibiting comparable performance and microstructure development. BP is expected to have low to free value in terms of cost since it is a by-product of the grinding process used to produce accurate dimensions for mortar-free walling in making calibrated brick components (Navrátilová and Rovnaníková, 2016). Considering the better mechanical behaviour obtained when increasing BP content, mixtures with the highest substitution ratios (i.e., 50% and 60%) were selected for natural aggregate replacement in phase II.

3.2. Effect of replacing natural aggregates with brick aggregates

Table 3 presents the flexural and compressive strength results of the 0BP, 50BP, and 60BP mixes with increasing replacement levels of natural aggregate with BA. All the mixtures had a CoV less than 7.8% for flexural and less than 5.2% for compression. Incorporating brick aggregate (BA) enhanced flexural strength performance as shown in the table. For example, the 50BP mix containing 30% or 50% BA exhibited almost 27% higher flexural strength than the mix without aggregate replacement and around 13% higher than the control (0BP). At 70% BA, flexural strength was comparable to the control (0BP) but remained around 15% higher than the mix without replacement. For 60BP, replacing 30% of natural aggregate with BA increased flexural strength to a similar level to the reference (0BP) and was around 28% higher than the mix without replacement. Increasing aggregate replacement to 50% and 70% BA resulted in 10% lower flexural strength than the reference (0BP) but 16% higher than the mix without aggregate replacement. The compressive strength of the 50BP mix did not change when up to 50% natural aggregate was replaced with BA. However, 50BP-70BA achieved similar compressive strength to the control (0BP) and 17% higher compressive strength than the mix without replacement. Similarly, the compressive strength of 60BP did not change when 30% natural

aggregate was replaced with BA. However, the 60BP-50BA and 60BP-70BA mixes achieved similar compressive strength to the control (0BP) and around 5–8% higher compressive strength than the mix without replacement. It is also worth noting that replacing natural aggregate with BA had a negligible effect on the composites' density. That is due to the comparable densities of natural aggregate (1.82 g cm^{-3}) and BA (1.981 g cm^{-3}), as shown in Table 3.The compressive strength of the cementitious composite is affected directly by the physical and textural properties of the aggregates (Xing et al., 2015). The improved mechanical performance of mixtures containing BA could be due to the porous and irregular surface texture of BA (see Fig. 3) that enhances the adhesion between aggregate particles and the paste matrix. This is supported by SEM observations (Fig. 9) which show good bonding between BA particles and paste matrix in 60P70BA. From Fig. 9, the embedment of BA in the paste matrix can be seen clearly without delamination or debonding at the aggregate-paste interface. The strong adhesion and good interlocking of BA with the cement paste allowed effective stress transfer when subjected to external loading, thereby improving the overall mechanical performance. Another reason could be the slightly higher porosity of BA than natural aggregate that absorbed part of the free water and enhanced the compactness of the mixture, increasing the mechanical property. In addition, the larger particle size distribution of BA (d50 < 800 μm) compared to natural aggregate (d50 < 300 μm), as shown in Fig. 3c, could also be responsible for the improvement in the strength. It is well known that increasing the maximum particle size of aggregates increases the compressive strength of resultant cementitious mixture (Donza et al., 2002; Siregar et al., 2017).

Fig. 10 presents the MIP results for 60BP and 60BP-70BA. The incorporation of BA increases the total intruded volume, thereby indicating a higher porosity (Fig. 10a). Nevertheless, the dominant peak pore size for 60BP-70BA was around 0.4 μm, compared to 0.6 μm in 60BP (Fig. 10b), indicating a finer pore size distribution in the 60BP-70BA composite. That could be due to the slightly higher water absorption capacity of BA [i.e., 9.8] than natural aggregate [i.e., 8], which decreased the free water/binder ratio, and thus resulting in a denser microstructure of the paste matrix. This could explain the slight enhancement in the mechanical performance of the mixtures prepared with BA.

The effect of replacing natural aggregate with BA on the reaction kinetics of one-part AAM was investigated using isothermal calorimetry. The results (Fig. 11) show a reduction in heat flow and cumulative heat released with increasing BA percentage. The lower intensity and the delay in appearance of the main exothermic peaks (I and II) with an increasing BA (Fig. 11a) could be due to the porous nature of BA that tends to absorb slightly higher amounts of water from the mixture compared to the natural aggregates, resulting in a reduction in the free water available for the initial dissolution of the precursor. This will, in turn, delay the formation of reaction products and, therefore, the acceleration peak (II). Another reason could be the Na$^+$ ions movement restriction due to the lower free water content because of the excessive absorption of BA, which slows down the geopolymerisation process. Fig. 11b shows a reduction in the total heat released after 72 h, indicating a lower degree of reaction with increasing BA content. Nevertheless, a slight strength enhancement was observed (as described in the preceding paragraphs), which is associated with a more densified microstructure in the presence of BA.

The above-presented results indicate the suitability of completely replacing natural aggregates with BA without showing noticeable differences in one-part AAM properties. Based on the findings above and considering the good performance obtained, the mixture with the highest binder and aggregate replacement level (60P70BA) was selected to study the effect of incorporating nano-graphite platelets in phase III.
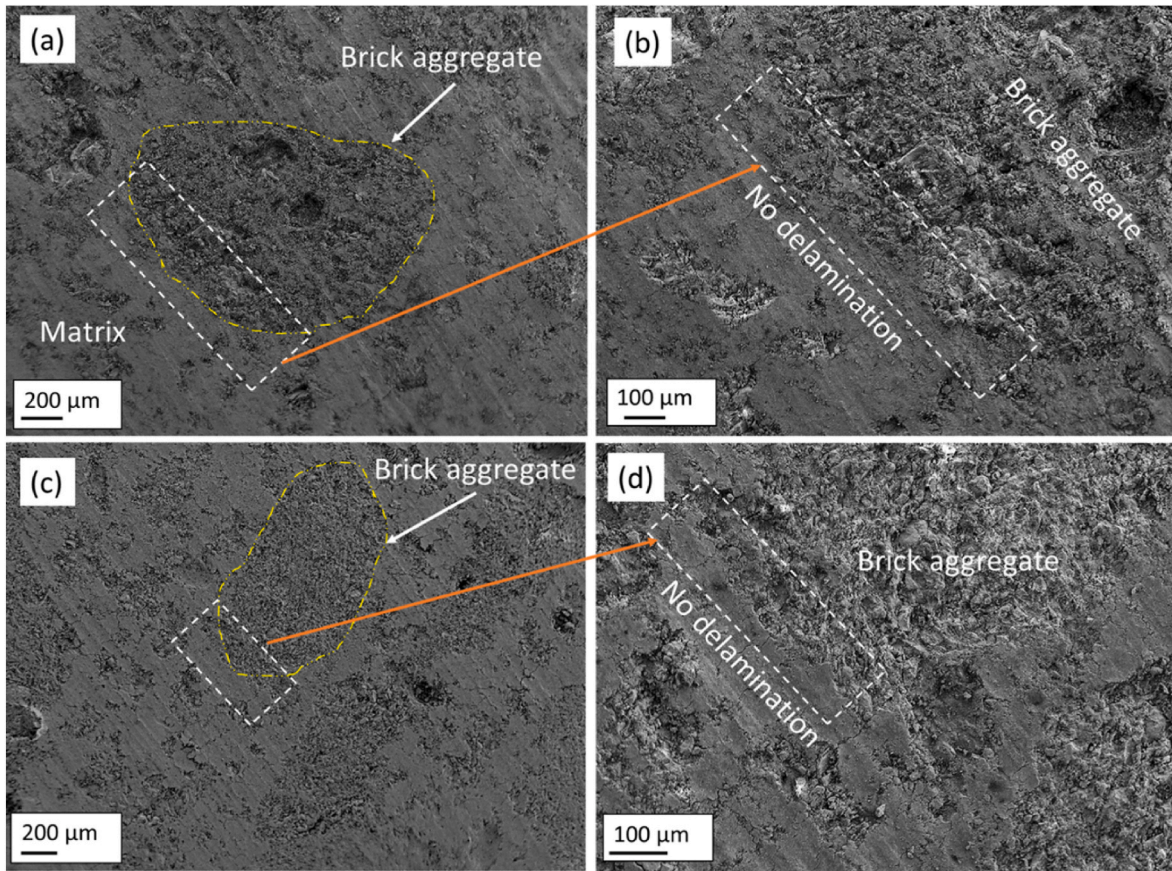
Table 3
Effect of different aggregate replacement levels on the flexural strength, compressive strength and density.

Mix ID	Flexural strength (MPa)	Compressive strength (MPa)	Density (g. cm^{-3})
0BP	7.5 ± 0.4	41.1 ± 1.3	1.995
50BP0BA	6.9 ± 0.4	35.2 ± 0.6	2.037
50BP30BA	8.5 ± 0.4	34.3 ± 1.7	2.047
50BP50BA	8.5 ± 0.4	35.1 ± 1.6	2.057
50BP70BA	7.7 ± 0.4	40.9 ± 1.6	2.070
60BP0BA	6.6 ± 0.4	38.2 ± 0.5	2.043
60BP30BA	7.5 ± 0.4	38.4 ± 0.2	2.048
60BP50BA	6.8 ± 0.4	41.2 ± 1.6	2.049
60BP70BA	6.8 ± 0.4	40.3 ± 1.1	2.052

Fig. 9. SEM images showing the microstructure of 60P70BA cross section after flexural strength testing.
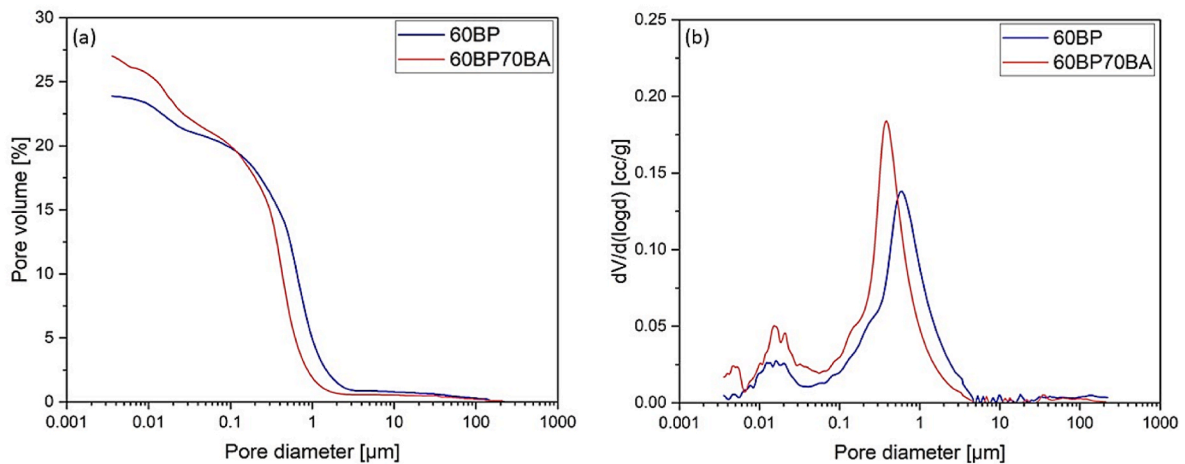

Fig. 10. (a) Cumulative intrusion and (b) pore size pore distribution from MIP for AAM with and without BA.

3.3. Effect of nano-graphite platelets

Fig. 12 shows that all mixtures modified with nG exhibited strength enhancement. Flexural strength increased by 31%, 37%, and 49% in mixes containing 0.1%, 0.5%, and 1% nG with a CoV of 3.2%, 1.5% and 4.9%, respectively, compared to the mix without nG with a CoV of 7.8% (Fig. 12a). Compressive strength increased by around 6% and 11% for the 0.1 nG and 1 nG mixes with a CoV of 0.98% and 2.69%, respectively, with similar performance for 0.5 nG with a CoV of 2.77% compared to the control that had a CoV of 2.77% (Fig. 12b). The strength enhancement is mainly due to crack-bridging phenomena caused by the presence

of nG in the microstructure of AAM (Chougan et al., 2020a). Furthermore, the distinct flaky shape and high fineness of nG particles facilitate their bonding with the cementitious matrix (Dong et al., 2021). The presence of stiff nG particles is expected to improve the mechanical performance of the composite, especially flexural strength, by controlling microcracking development and propagation induced by loading. Although incorporating 0.1% enhanced the compressive strength slightly, adding 1% did not show a significant difference compared to 0.1%. The slight enhancement could be due to the high surface area and morphology of nano-graphite platelets, which enhanced the mixtures' interconnected mechanism. However, the agglomeration effect after
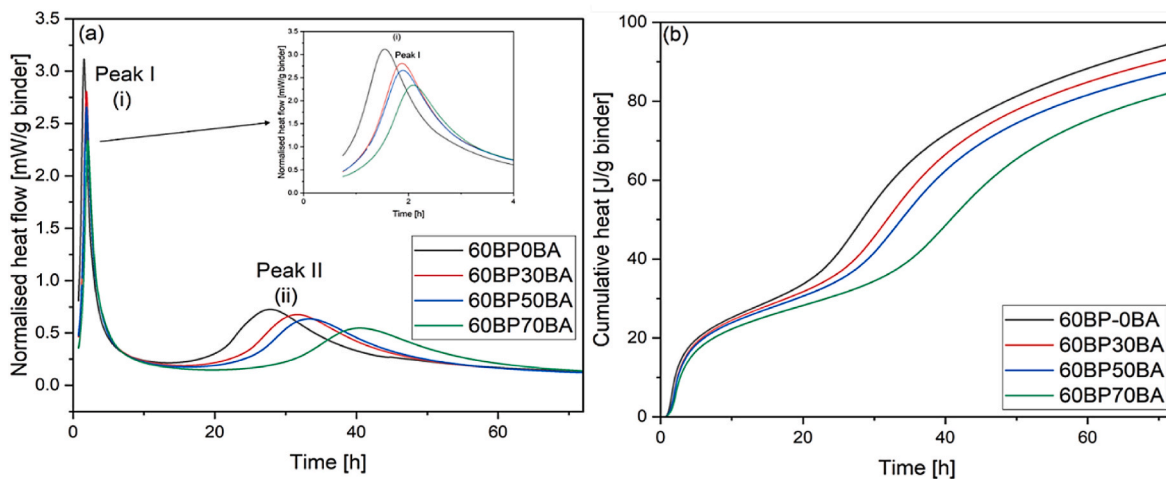
Fig. 11. Isothermal calorimetry curves of one-part AAMs with different BA percentages: (a) normalised heat flow and (b) cumulative heat release.
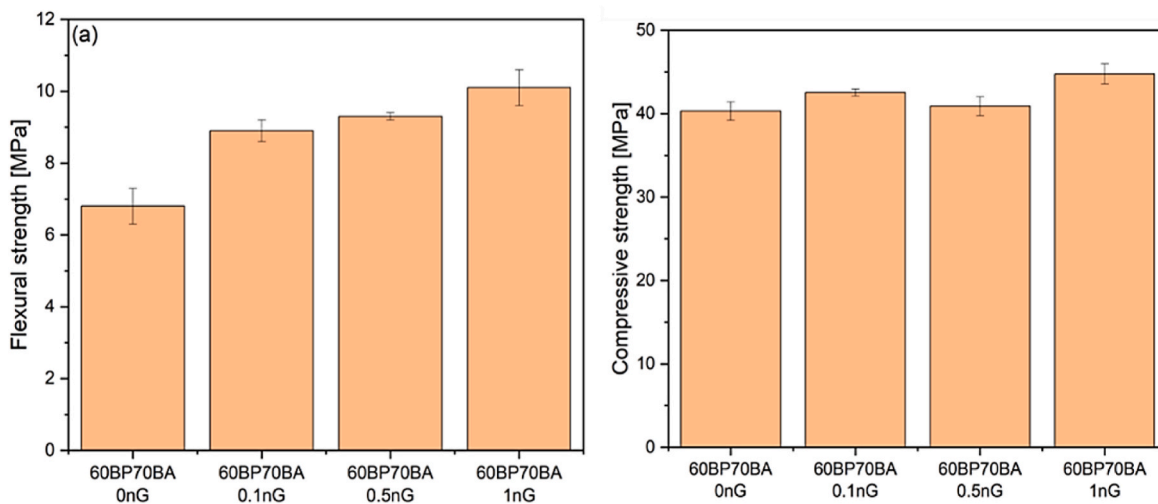

Fig. 12. Effect of different nG dosages on (a) flexural strength and (b) compressive strength. Error bars represent the standard deviation.

adding a high content of nanomaterials could limit the enhancement in the cementitious mixture. Fig. 13 provides SEM micrographs showing examples where the presence of nG particles has appeared to bridge/-block the propagation of microcracks. Chougan et al. (2020a) studied the effect of incorporating up to 1% nG in 3D-printed two-part geopolymers and reported similar behaviour, whereby compressive and flexural strength increased by 14% and 46%, respectively. Under compression, cracks initiate and propagate orthogonal to the local tensile stress and parallel to the loading direction. According to the authors, the improved strength is attributed to three mechanisms. First, the nG particles mitigate stress concentrations in the matrix due to their high elastic modulus and spatial distribution. That helps in spreading stresses over a larger region and prevents localised failure. Second, the crack-blocking/bridging effect of nG prolongs the initiation and delays the propagation of cracks. Crack intersecting nG will require higher fracture energy to propagate through (Ranjbar et al., 2015). The third mechanism is the additional (C-A-S-H) gel formed due to greater nucleation sites offered by the nG particles (Bellum et al., 2020; Long et al., 2019).

3.4. Water absorption

Fig. 14 presents the water absorption for the control (0BP), 60BP, 60P70BA, and 60P70BA with different nG dosages. The incorporation of brick in the mixture increased water absorption due to its highly porous structure. The considerable difference between 0BP and mixtures prepared with BP and BA at the early stages of the test is due to the high capillary absorption of brick (Li et al., 2022). Another interesting observation is that 60BP reached full saturation after 60 min compared to 6 h for the control (0BP), yet both mixes exhibited similar water absorption of around 14%. This is in good agreement with MIP results (Fig. 6) that showed that both mixes had similar total porosity while 60BP had a finer pore size distribution (and therefore greater capillary suction). Incorporating 70% BA increased total water absorption to around 15.5%, mainly due to the higher porosity and absorption of BA compared to natural aggregate (Fig. 10a). Incorporating nano-graphite platelets significantly improved the resistance to water absorption and reached values lower than the control (0BP). 60P70BA-0.1 nG attained the lowest absorption, with a reduction of 102% and 18% after 5 min and 72 h, respectively, compared to the mix without nG (60P70BA). The remarkable reduction in water absorption for mixes with nG can be attributed to the hydrophobic nature of nano-graphite particles, which act as a transport barrier and inhibit water ingress into AAM (Du and Pang, 2015). Chougan et al. (2020b) found that incorporating 0.2% nG lowered the water absorption values by 80%. Dua et al. (Du and Pang, 2015) showed that incorporating 5% nano-graphene decreased the average water absorption by 75%. However, this study showed that water absorption increased at nG dosages higher than 0.1%. For
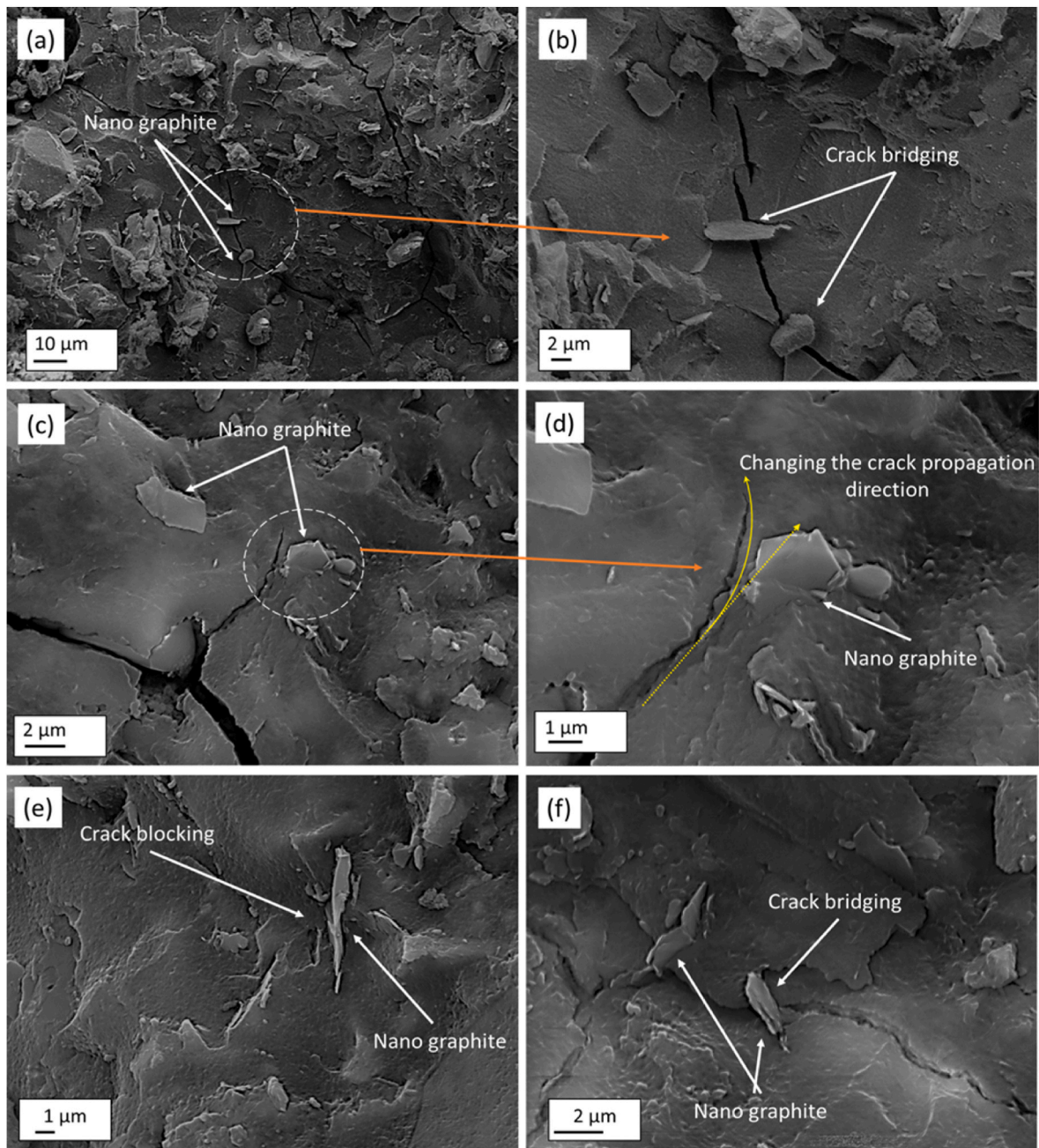
Fig. 13. Microstructure of 60P70BA with 1% nG addition after flexural strength test.

example, the mix with 1% nG displayed significantly increased water absorption values comparable to that without nG (60P70BA). This could be due to poor dispersion causing agglomeration and clustering of excess nG particles, thus reducing its overall effectiveness (Indukuri and Nerella, 2021; Fu et al., 2020).

3.5. Freeze-thaw resistance

Fig. 15 shows that the AAMs experienced compressive strength reduction ranging from 5 to 55% after exposure to freeze-thaw (FT) cycles. It is interesting to note that the control (0BP) suffered the highest strength reduction (55%), while mixes incorporating BP, BA, and nG showed a lower reduction in compressive strength after completing the FT cycles. The main reason for the strength reduction following the freeze-thaw cycles is the crack initiation during freeze cycles. During the freezing process, entrapped water expands as a result of transforming

into ice, which leads to the widening and rupturing of the pore structure of the AAM, thus, deteriorating the mechanical performance. Hence, the damage induced by FT cycles varies depending on the free water present in the system (Wang et al., 2023). In other words, the higher the water absorption level of the mixture, the higher the strength loss. According to Guo et al. (2017), replacing FA with BP significantly reduced pore size and total porosity. The volume and size of pores affect durability (Ozcan, 2021). For example, a finer pore structure reduces water ingress, resulting in better resistance to FT (Lu et al., 2021). In this study, the fewer pores in the 30–300 nm range and the slightly lower porosity in 60BP (Fig. 6b) could explain its better resistance to FT compared to 0BP. Moreover, the more densified microstructure when incorporating BA than 60BP, as revealed by MIP (Fig. 10), can explain the better performance in the FT test. In addition, better resistance could be associated with the porous structure of BA that offers space for expansive mechanisms of freezing water to relieve the pressure induced by ice formation.
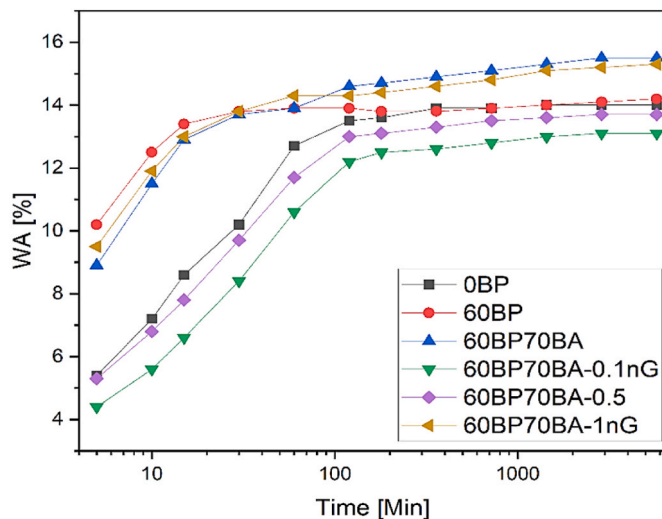
Fig. 14. Water absorption results of the different mixtures.

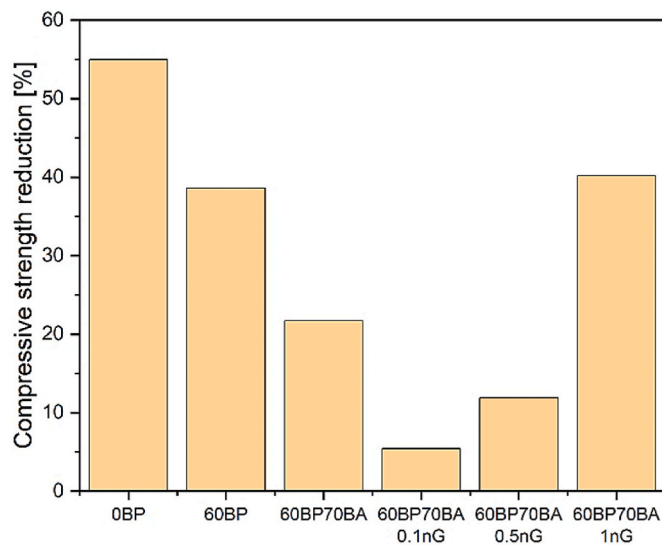**Fig. 16.** Fire resistance of one-part geopolymer mixes.

Fig. 15. Compressive strength loss after freeze-thaw test.

The mix containing 0.1% nG showed the best performance with a compressive strength reduction of only 5%. The presence of hydrophobic nG decreases water absorption and, thus, less ice formation. In addition, the crack-bridging effect of nG helps to control crack initiation and propagation induced by water expansion during the freezing process. However, increasing the nano-graphite dosage degrades the resistance to FT, which is in line with the higher water absorption observed in Fig. 14, which increases the amount of freezable water (Ebrahimi et al., 2018). Moreover, the mass loss of all mixtures was within the standard deviation range.

3.6. Fire resistance

The reduction percentage in compressive strength after exposing the specimens to a temperature of 800 °C for 1 h are presented in Fig. 16. The highest strength reduction of around 21% was observed for the mix prepared with 1% nG, which had a compressive strength value of 36.4 MPa after being exposed to elevated temperature. It can be notice that control mix (0BP) showed significantly higher reduction compared to the mixtures prepared with brick powder (BP) and brick aggregates (BA). The results indicated that the incorporation of brick in powder and
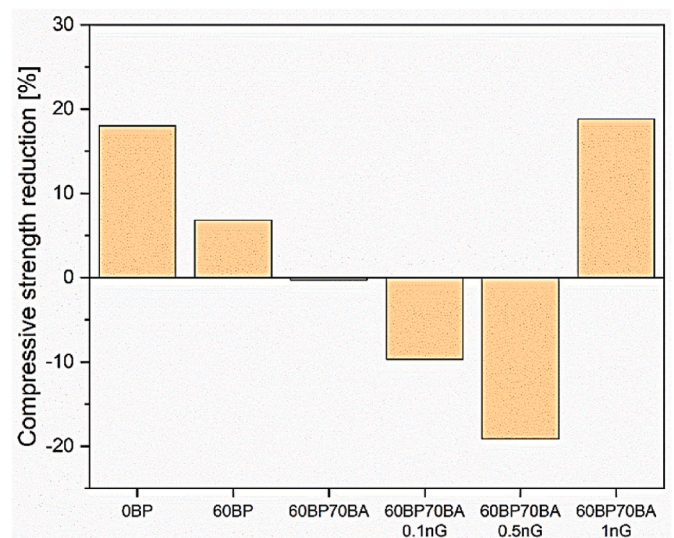
aggregate form enhanced the fire resistivity of the mixture. That is in good agreement with the results reported in (Giannopoulou et al., 2023). Giannopoulou et al. (2023) measured the compressive strength reduction of two-part waste brick-based geopolymer when exposed to 800 °C for 2 h and did not observe any reduction in the strength. The authors suggest that the observed behaviour in the compressive strength of brick geopolymers after exposure to elevated temperatures resulted from structural rearrangements in their matrices caused by water evaporation, dehydroxylation, and phase transformations (Ahmad et al., 2022; van Deventer et al., 2007; He et al., 2020). The water evaporation and the loss of structural water could result in the initiation of micro-cracks, which can weaken the structure and decrease the compressive strength of the mixtures (Sun et al., 2013). However, the lower reduction in the case of mixes prepared with BP could be due to the high absorption capacity of the porous brick particles, which possibly decreased the micro-crack growth due to less water evaporation from the system. That, in turn, could also explain the further enhancement of fire resistivity when incorporating BA, in addition to BA's rough and porous surface that provided better interlocking and required higher pressure for micro-crack development. The compressive strength performance of mixtures prepared with 0.1% and 0.5% nG increased after exposure to heat, which can be attributed to more geopolymerisation reactions occurring in the geopolymer after being heated. That is in good agreement with the results reported in (Abd Razak et al., 2022; Kodur and Phan, 2007; Sarker et al., 2014). However, for the mix prepared with 1% nG, the significant reduction in compressive strength can be due to the excessive addition of nG that prevented the complete dispersion of the particles, resulting in agglomeration and clustering of the particles which reduces its overall effectiveness (Indukuri and Nerella, 2021; Fu et al., 2020). In addition, the unreacted and poorly dispersed excessive nG worked on absorbing water and led to a drier mixture due to the high specific area of nG particles. This also leads to a less densified mix. That, in turn, would facilitate the growth of micro-cracks when exposed to elevated temperature and reduce the compressive performance of the mixture. It can be indicated from the results that end-of-life brick in powder form as binder could be used to produce fire-resistant geopolymer, and up to 0.5% nG could be incorporated to further modify the fire resistivity of the mixture.

4. Conclusions

This study investigated the effects of end-of-life waste brick on the properties and performance of one-part alkali-activated materials

(AAM). Brick was used in powder form to partially replace fly ash precursor and in aggregate form to partially replace natural aggregate. The mixture with the highest substitutions of brick powder (60%) and brick aggregate (70%) was further modified by incorporating 0.1–1% nano-graphite additive. The one-part AAMs' mechanical performance, reaction kinetics, microstructure, water absorption, and freeze-thaw durability were studied. The following conclusions were drawn:

- Brick powder is reactive and can completely replace fly ash in one-part AAM. This produced lower compressive strength (6–20%) and flexural strength (6–15%) but similar total porosity and water absorption. Moreover, an improved freeze-thaw resistance was observed compared to fly ash-based one-part AAM. Furthermore, brick-based AAM had better fire resistivity with only 6% compressive strength reduction.
- Replacing natural aggregate with brick aggregate improved compressive strength (up to 17%), flexural strength (up to 27%) and freeze-thaw resistance. It also enhanced the fire resistivity of the composite, showing no reduction in compressive strength. This is due to the irregular surface texture of brick aggregate that gave better adhesion with the paste matrix and denser aggregate-paste interface. However, its incorporation increased water absorption due to the porous nature of brick aggregate relative to natural aggregate.
- Brick-based AAM had a similar pore structure to FA-based AAM and was found to release higher heat due to the high silica in brick powder. Incorporating BA resulted in pore structure refinement of the paste compared to natural aggregate. However, total porosity increased slightly due to the porous nature of brick aggregate.
- The addition of 0.1% nano-graphite enhanced compressive strength by 6% and increased flexural strength considerably by 31% through its crack-blocking/bridging mechanism. Furthermore, nano-graphite decreased water absorption by 18% and improved freeze-thaw durability due to its hydrophobic nature. Moreover, nano-graphite addition modified the mixtures' fire resistivity, allowing the AAM to gain more strength rather than a reduction compared to before exposure to elevated temperature. However, increasing the nano-graphite dosage led to degraded performance, presumably due to a lack of dispersion of particles and agglomeration within the AAM matrix.

Overall, this study succeeded in upcycling bricks obtained from construction sites and re-using them as construction materials in different forms. Additional research on the influence of completely replacing natural aggregate with brick aggregate, and the effect of incorporating different additives on long-term durability properties, is needed.

Declaration of competing interest

The authors declare that they have no known competing financial interests or personal relationships that could have appeared to influence the work reported in this paper.

Data availability

Data will be made available on request.

Acknowledgement

References

Abd Razak, S.N., Shafiq, N., Hasan Nikbakht, E., Mohammed, B.S., Guillaumat, L., Farhan, S.A., 2022. Fire performance of fly-ash-based geopolymer concrete: effect of burning temperature on mechanical and microstructural properties, Mater. Today Proc 66, 2665–2669. https://doi.org/10.1016/j.matpr.2022.06.491.

Ahmad, R., Ibrahim, W.M.W., Abdullah, M.M.A.B., Pakawanit, P., Vizureanu, P., Abdullah, A.S., Sandu, A.V., Ahmad Zaidi, F.H., 2022. Geopolymer-based nepheline ceramics: effect of sintering profile on morphological characteristics and flexural strength. Crystals 12, 1–9. https://doi.org/10.3390/cryst12091313.

Akis, Y.A.A.T., 2023. Influence of cement replacement by calcinated kaolinitic and montmorillonite clays on the properties of mortars. Arabian J. Sci. Eng. https://doi.org/10.1007/s13369-023-08041-y.

Al-noaimat, Y.A., Chougan, M., Al-kheetan, M.J., Al-mandhari, O., Al-saidi, W., Al-maqbali, M., Al-hosni, H., Hamidreza, S., 2023a. 3D printing of limestone-calcined clay cement : a review of its potential implementation in the construction industry. Results Eng 18, 101115. https://doi.org/10.1016/j.rineng.2023.101115.

Al-noaimat, Y.A., Hamidreza, S., Chougan, M., Al-kheetan, M.J., 2023b. A review of 3D printing low-carbon concrete with one-part geopolymer : engineering , environmental and economic feasibility. Case Stud. Constr. Mater. 18, e01818 https://doi.org/10.1016/j.cscm.2022.e01818.

Álvarez-Ayuso, E., Querol, X., Plana, F., Alastuey, A., Moreno, N., Izquierdo, M., Font, O., Moreno, T., Diez, S., Vázquez, E., Barra, M., 2008. Environmental, physical and structural characterisation of geopolymer matrixes synthesised from coal (co-) combustion fly ashes. J. Hazard Mater. 154, 175–183. https://doi.org/10.1016/j.jhazmat.2007.10.008.

Arif, R., Khitab, A., Serkan, M., Bilal, R., Khan, N., 2021. Case Studies in Construction Materials Experimental analysis on partial replacement of cement with brick powder in concrete. Case Stud. Constr. Mater. 15, e00749 https://doi.org/10.1016/j.cscm.2021.e00749.

Bayraktar, O.Y., Citoglu, G.S., Belgin, C.M., Cetin, S., Cetin, M., 2019a. Investigation of Effect of Brick Dust and Silica Fume on the Properties of Portland Cement Mortar.

Bayraktar, O.Y., Citoglu, G.S., Belgin, C.M., Cetin, M., 2019b. INVESTIGATION OF THE MECHANICAL PROPERTIES OF MARBLE DUST AND SILICA FUME SUBSTITUTED PORTLAND CEMENT SAMPLES UNDER HIGH.

Bellum, R.R., Muniraj, K., Indukuri, C.S.R., Madduru, S.R.C., 2020. Investigation on performance enhancement of fly ash-GGBFS based graphene geopolymer concrete. J. Build. Eng. 32, 101659 https://doi.org/10.1016/j.jobe.2020.101659.

BS 1881-122, 2011. Testing Concrete - Part 122: Method for Determination of Water Absorption n.d.).

BS EN 1015-3, 1999. Methods of Test for Mortar for Masonry- Part 3: Determination of Consistence of Fresh Mortar (By Flow Table) n.d.

BS EN 15167-1, 2006. Ground Granulated Blast Furnace Slag for Use in Concrete, Mortar and Grout - Part 1: Definitions, Specifications and Conformity Criteria, n.d. (n.d.).

BS EN 196-1, 2016. Methods of Testing Cement - Part 1. Determination of cement n.d.).

BS EN 450-1, 2012. Fly Ash for Concrete - Part 1: Definitions. specifications and conformity criteria (n.d.).

Chindaprasirt, P., Chareerat, T., Hatanaka, S., Cao, T., 2011. High-strength geopolymer using high-calcium fly ash. J. Mater. Civ. Eng. 23, 264–270. https://doi.org/10.1061/(asce)mt.1943-5533.0000161.

Chougan, M., Marotta, E., Lamastra, F.R., Vivio, F., Montesperelli, G., Ianniruberto, U., Bianco, A., 2019. A systematic study on EN-998-2 premixed mortars modified with graphene-based materials. Construct. Build. Mater. 227, 116701 https://doi.org/10.1016/j.conbuildmat.2019.116701.

Chougan, M., Hamidreza Ghaffar, S., Jahanzat, M., Albar, A., Mujaddedi, N., Swash, R., 2020a. The influence of nano-additives in strengthening mechanical performance of 3D printed multi-binder geopolymer composites. Construct. Build. Mater. 250, 118928 https://doi.org/10.1016/j.conbuildmat.2020.118928.

Chougan, M., Marotta, E., Lamastra, F.R., Vivio, F., Montesperelli, G., Ianniruberto, U., Hamidreza Ghaffar, S., Al-kheetan, M.J., Bianco, A., 2020b. High performance cementitious nanocomposites: the effectiveness of nano-Graphite (nG). Construct. Build. Mater. 259, 119687 https://doi.org/10.1016/j.conbuildmat.2020.119687.

Criado, M., Fernández-Jiménez, A., Palomo, A., 2007. Alkali activation of fly ash: effect of the SiO2/Na2O ratio. Part I: FTIR study. Microporous Mesoporous Mater. 106, 180–191. https://doi.org/10.1016/j.micromeso.2007.02.055.

Dadsetan, S., Siad, H., Lachemi, M., Sahmaran, M., 2019. Construction and demolition waste in geopolymer concrete technology: a review. Mag. Concr. Res. 71, 1232–1252. https://doi.org/10.1680/jmacr.18.00307.

Dang, J., Zhao, J., Hu, W., Du, Z., Gao, D., 2018. Properties of mortar with waste clay bricks as fine aggregate. Construct. Build. Mater. 166, 898–907. https://doi.org/10.1016/j.conbuildmat.2018.01.109.

Dimov, D., Amit, I., Gorrie, O., Barnes, M.D., Townsend, N.J., Neves, A.I.S., Withers, F., Russo, S., Craciun, M.F., 2018. In: Ultrahigh Performance Nanoengineered Graphene – Concrete Composites for Multifunctional Applications, 1705183. https://doi.org/10.1002/adfm.201705183.

Dong, Q., Wan, L., Luan, C., Wang, J., Du, P., 2021. Effect of graphene oxide on properties of alkali-activated slag. Materials 14, 1–13. https://doi.org/10.3390/ma14206107.

Donza, H., Cabrera, O., Irassar, E.F., 2002. High-strength concrete with different fine aggregate. Cement Concr. Res. 32, 1755–1761. https://doi.org/10.1016/S0008-8846(02)00860-8.

Du, H., Pang, S.D., 2015. Enhancement of barrier properties of cement mortar with graphene nanoplatelet. Cement Concr. Res. 76, 10–19. https://doi.org/10.1016/j.cemconres.2015.05.007.

Duxson, P., Provis, J.L., Lukey, G.C., van Deventer, J.S.J., 2007. The role of inorganic polymer technology in the development of "green concrete,". Cement Concr. Res. 37, 1590–1597. https://doi.org/10.1016/j.cemconres.2007.08.018.

Ebrahimi, K., Daiezadeh, M.J., Zakertabrizi, M., Zahmatkesh, F., Habibnejad Korayem, A., 2018. A review of the impact of micro- and nanoparticles on freeze-thaw durability of hardened concrete: mechanism perspective. Construct. Build. Mater. 186, 1105–1113. https://doi.org/10.1016/j.conbuildmat.2018.08.029.

El-seidy, E., Sambucci, M., Chougan, M., Al-kheetan, M.J., 2022. Mechanical and physical characteristics of alkali- activated mortars incorporated with recycled polyvinyl chloride and rubber aggregates. J. Build. Eng. 60, 105043 https://doi.org/10.1016/j.jobe.2022.105043.

El-seidy, E., Chougan, M., Sambucci, M., Al-kheetan, M.J., Biblioteca, I, Valente, M., Hamidreza, S., 2023. Lightweight alkali-activated materials and ordinary Portland cement composites using recycled polyvinyl chloride and waste glass aggregates to fully replace natural sand. Construct. Build. Mater. 368, 130399 https://doi.org/10.1016/j.conbuildmat.2023.130399.

Erfanimanesh, A., Sharbatdar, M.K., 2020. Mechanical and microstructural characteristics of geopolymer paste, mortar, and concrete containing local zeolite and slag activated by sodium carbonate. J. Build. Eng. 32, 101781 https://doi.org/10.1016/j.jobe.2020.101781.

Fadeel, B., Bussy, C., Merino, S., Vázquez, E., Flahaut, E., Mouchet, F., Evariste, L., Gauthier, L., Koivisto, A.J., Vogel, U., Martín, C., Delogu, L.G., Buerki-Thurnherr, T., Wick, P., Beloin-Saint-Pierre, D., Hischier, R., Pelin, M., Candotto Carniel, F., Tretiach, M., Cesca, F., Benfenati, F., Scaini, D., Ballerini, L., Kostarelos, K., Prato, M., Bianco, A., 2018. Safety assessment of graphene-based materials: focus on human health and the environment. ACS Nano 12, 10582–10620. https://doi.org/10.1021/acsnano.8b04758.

Fu, C., Xie, C., Liu, J., Wei, X., Wu, D., 2020. A comparative study on the effects of three nano-materials on the properties of cement-based composites. Materials 13. https://doi.org/10.3390/ma13040857.

Giannopoulou, I., Robert, P.M., Sakkas, K.M., Petrou, M.F., Nicolaides, D., 2023. High temperature performance of geopolymers based on construction and demolition waste. J. Build. Eng. 72, 106575 https://doi.org/10.1016/j.jobe.2023.106575.

Guo, X., Shi, H., Wei, X., 2017. Pore properties , inner chemical environment , and microstructure of nano-modi fi ed CFA-WBP (class C fly ash-waste brick powder) based geopolymers. Cem. Concr. Compos. 79, 53–61. https://doi.org/10.1016/j.cemconcomp.2017.01.007.

He, R., Dai, N., Wang, Z., 2020. Thermal and mechanical properties of geopolymers exposed to high temperature: a literature review, 2020 Adv. Civ. Eng.. https://doi.org/10.1155/2020/7532703.

Hwang, C.L., Yehualaw, M.D., Vo, D.H., Huynh, T.P., Largo, A., 2019. Performance evaluation of alkali activated mortar containing high volume of waste brick powder blended with ground granulated blast furnace slag cured at ambient temperature. Construct. Build. Mater. 223, 657–667. https://doi.org/10.1016/j.conbuildmat.2019.07.062.

Indukuri, C.S.R., Nerella, R., 2021. Enhanced transport properties of graphene oxide based cement composite material. J. Build. Eng. 37 https://doi.org/10.1016/j.jobe.2021.102174.

Juenger, M.C.G., Winnefeld, F., Provis, J.L., Ideker, J.H., 2011. Advances in alternative cementitious binders. Cement Concr. Res. 41, 1232–1243. https://doi.org/10.1016/j.cemconres.2010.11.012.

Kodur, V.K.R., Phan, L., 2007. Critical factors governing the fire performance of high strength concrete systems. Fire Saf. J. 42, 482–488. https://doi.org/10.1016/j.firesaf.2006.10.006.

Li, L., Liu, W., You, Q., Chen, M., Zeng, Q., Zhou, C., Zhang, M., 2020. Relationships between microstructure and transport properties in mortar containing recycled ceramic powder. J. Clean. Prod. 263 https://doi.org/10.1016/j.jclepro.2020.121384.

Li, Y., Shen, J., Lin, H., Lv, J., Feng, S., Ci, J., 2022. Properties and environmental assessment of eco-friendly brick powder geopolymer binders with varied alkali dosage. J. Build. Eng. 58, 105020 https://doi.org/10.1016/j.jobe.2022.105020.

Liu, Q., Xu, Q., Yu, Q., Gao, R., Tong, T., 2016. Experimental investigation on mechanical and piezoresistive properties of cementitious materials containing graphene and graphene oxide nanoplatelets. Construct. Build. Mater. 127, 565–576. https://doi.org/10.1016/j.conbuildmat.2016.10.024.

Liu, T., Wang, Z., Zou, D., Zhou, A., Du, J., 2019. Strength enhancement of recycled aggregate pervious concrete using a cement paste redistribution method. Cement Concr. Res. 122, 72–82. https://doi.org/10.1016/j.cemconres.2019.05.004.

Long, W.J., Ye, T.H., Luo, Q.L., Wang, Y., Mei, L., 2019. Reinforcing mechanism of reduced graphene oxide on flexural strength of geopolymers: a synergetic analysis of hydration and chemical composition. Nanomaterials 9. https://doi.org/10.3390/nano9121723.

Lu, W., 2019. Big data analytics to identify illegal construction waste dumping: a Hong Kong study. Resour. Conserv. Recycl. 141, 264–272. https://doi.org/10.1016/j.resconrec.2018.10.039.

Lu, Z., Feng, Z., Yao, D., Li, X., Ji, H., 2021. Freeze-thaw resistance of Ultra-High performance concrete : dependence on concrete composition. Construct. Build. Mater. 293, 123523 https://doi.org/10.1016/j.conbuildmat.2021.123523.

Ma, Z., Tang, Q., Wu, H., Xu, J., Liang, C., 2020. Mechanical properties and water absorption of cement composites with various fineness and contents of waste brick powder from C & D waste, Cem. Concr. Compos. 114, 103758 https://doi.org/10.1016/j.cemconcomp.2020.103758.

Ma, G., Yan, Y., Zhang, M., Sanjayan, J., 2022. Effect of steel slag on 3D concrete printing of geopolymer with quaternary binders. Ceram. Int. https://doi.org/10.1016/j.ceramint.2022.05.305.

Mackenzie, K.J.D., Bolton, Æ.M.J., 2009. In: Electrical and Mechanical Properties of Aluminosilicate Inorganic Polymer Composites with Carbon Nanotubes https://doi.org/10.1007/s10853-009-3377-z, 2851–2857.

Migunthanna, J., Rajeev, P., Sanjayan, J., 2021. Investigation of waste clay brick as partial replacement of geopolymer binders for rigid pavement application. Construct. Build. Mater. 305, 124787 https://doi.org/10.1016/j.conbuildmat.2021.124787.

Navrátilová, E., Rovnaníková, P., 2016. Pozzolanic properties of brick powders and their effect on the properties of modified lime mortars. Construct. Build. Mater. 120, 530–539. https://doi.org/10.1016/j.conbuildmat.2016.05.062.

Ozcan, A., 2021. Effect of Binder Content and Recycled Concrete Aggregate on Freeze-Thaw and Sulfate Resistance of GGBFS Based Geopolymer Concretes, p. 301. https://doi.org/10.1016/j.conbuildmat.2021.124246.

Pandey, A., Kumar, B., 2019. Evaluation of water absorption and chloride ion penetration of rice straw ash and microsilica admixed pavement quality concrete. Heliyon 5, e02256. https://doi.org/10.1016/j.heliyon.2019.e02256.

Papanikolaou, I., Arena, N., Al-tabbaa, A., 2021. Graphene nanoplatelet reinforced concrete for self-sensing structures e A lifecycle assessment perspective. J. Clean. Prod. 240, 118202 https://doi.org/10.1016/j.jclepro.2019.118202.

Paul, S.C., Babafemi, A.J., Anggraini, V., Rahman, M.M., 2018. Properties of normal and recycled brick aggregates for production of medium range (25-30 MPa) structural strength concrete. Buildings 8. https://doi.org/10.3390/BUILDINGS8050072.

PN-85/B-04500, 1985. Construction Mortars. Research of Physical and Strength Characteristics. n.d.. Polish committee for standardization, Warsaw, Poland.

Ranjbar, N., Mehrali, M., Mehrali, M., Alengaram, U.J., Jumaat, M.Z., 2015. Graphene nanoplatelet-fly ash based geopolymer composites. Cement Concr. Res. 76, 222–231. https://doi.org/10.1016/j.cemconres.2015.06.003.

Robayo, R.A., Mulford, A., Munera, J., Mejía de Gutiérrez, R., 2016. Alternative cements based on alkali-activated red clay brick waste. Construct. Build. Mater. 128, 163–169. https://doi.org/10.1016/j.conbuildmat.2016.10.023.

Robert, C., 2020. Transition to circular economy in the construction industry. Environmental aspects of waste brick recycling scenarios 118, 510–520. https://doi.org/10.1016/j.wasman.2020.09.004.

Rovnaník, P., Rovnaníková, P., Vyšvařil, M., Grzeszczyk, S., Janowska-Renkas, E., 2018. Rheological properties and microstructure of binary waste red brick powder/metakaolin geopolymer. Construct. Build. Mater. 188, 924–933. https://doi.org/10.1016/j.conbuildmat.2018.08.150.

Sarker, P.K., Kelly, S., Yao, Z., 2014. Effect of fire exposure on cracking, spalling and residual strength of fly ash geopolymer concrete. Mater. Des. 63, 584–592. https://doi.org/10.1016/j.matdes.2014.06.059.

Siregar, A.P.N., Rafiq, M.I., Mulheron, M., 2017. Experimental investigation of the effects of aggregate size distribution on the fracture behaviour of high strength concrete. Construct. Build. Mater. 150, 252–259. https://doi.org/10.1016/j.conbuildmat.2017.05.142.

Statements, B., Size, T., 2003. Standard Test Method for Density , Relative Density (Specific Gravity), and Absorption, pp. 1–6.

Sun, Z., Cui, H., An, H., Tao, D., Xu, Y., Zhai, J., Li, Q., 2013. Synthesis and thermal behavior of geopolymer-type material from waste ceramic. Construct. Build. Mater. 49, 281–287. https://doi.org/10.1016/j.conbuildmat.2013.08.063.

van Deventer, J.S.J., Provis, J.L., Duxson, P., Lukey, G.C., 2007. Reaction mechanisms in the geopolymeric conversion of inorganic waste to useful products. J. Hazard Mater. 139, 506–513. https://doi.org/10.1016/j.jhazmat.2006.02.044.

Wang, Y., Cao, Y., Zhang, P., Ma, Y., Zhao, T., Wang, H., Zhang, Z., 2019. Water absorption and chloride diffusivity of concrete under the coupling effect of uniaxial compressive load and freeze–thaw cycles. Construct. Build. Mater. 209, 566–576. https://doi.org/10.1016/j.conbuildmat.2019.03.091.

Wang, B., Yan, L., Fu, Q., Kasal, B., 2021. A comprehensive review on recycled aggregate and recycled aggregate concrete. Resour. Conserv. Recycl. 171, 105565 https://doi.org/10.1016/j.resconrec.2021.105565.

Wang, W., Zhong, Z., Kang, X., Ma, X., 2023. Physico-mechanical properties and micromorphological characteristics of graphene oxide reinforced geopolymer foam concrete. J. Build. Eng. 72, 106732 https://doi.org/10.1016/j.jobe.2023.106732.

Wong, C.L., Mo, K.H., Yap, S.P., Alengaram, U.J., Ling, T.C., 2018. Potential use of brick waste as alternate concrete-making materials: a review. J. Clean. Prod. 195, 226–239. https://doi.org/10.1016/j.jclepro.2018.05.193.

Wong, C.L., Mo, K.H., Alengaram, U.J., Yap, S.P., 2020a. Mechanical strength and permeation properties of high calcium fly ash-based geopolymer containing recycled brick powder. J. Build. Eng. 32, 101655 https://doi.org/10.1016/j.jobe.2020.101655.

Wong, C.L., Mo, K.H., Alengaram, U.J., Yap, S.P., 2020b. Mechanical strength and permeation properties of high calcium fly ash-based geopolymer containing recycled brick powder. J. Build. Eng. 32, 101655 https://doi.org/10.1016/j.jobe.2020.101655.

Xing, Z., Beaucour, A.L., Hebert, R., Noumowe, A., Ledesert, B., 2015. Aggregate's influence on thermophysical concrete properties at elevated temperature. Construct. Build. Mater. 95, 18–28. https://doi.org/10.1016/j.conbuildmat.2015.07.060.

Yusuf, M.O., Johari, M.A.M., Ahmad, Z.A., Maslehuddin, M., 2014. Effects of addition of Al(OH)3 on the strength of alkaline activated ground blast furnace slag-ultrafine palm oil fuel ash (AAGU) based binder. Construct. Build. Mater. 50, 361–367. https://doi.org/10.1016/j.conbuildmat.2013.09.054.

Zawrah, M.F., Gado, R.A., Feltin, N., Ducourtieux, S., Devoille, L., 2016. Recycling and utilization assessment of waste fired clay bricks (Grog) with granulated blast-furnace slag for geopolymer production. Process Saf. Environ. Protect. 103, 237–251. https://doi.org/10.1016/j.psep.2016.08.001.

Zhang, Z., Choy, Y., Arulrajah, A., Horpibulsuk, S., 2018. A review of studies on bricks using alternative materials and approaches. Construct. Build. Mater. 188, 1101–1118. https://doi.org/10.1016/j.conbuildmat.2018.08.152.

Zhang, B., Zhu, H., Cheng, Y., Huseien, G.F., Shah, K.W., 2022. Shrinkage mechanisms and shrinkage-mitigating strategies of alkali-activated slag composites: a critical review. Construct. Build. Mater. 318, 125993 https://doi.org/10.1016/j.conbuildmat.2021.125993.

Zheng, Q., Han, B., Cui, X., Yu, X., Ou, J., 2017. Graphene-engineered cementitious composites. Small makes a big impact 7, 1–18. https://doi.org/10.1177/1847980417742304.